Bioactive Materials 19 (2023) 282–291

Contents lists available at ScienceDirect

Bioactive Materials

journal homepage: www.keaipublishing.com/en/journals/bioactive-materials

Nanostructured polyvinylpyrrolidone-curcumin conjugates allowed for kidney-targeted treatment of cisplatin induced acute kidney injury

Hao Wei [a,c,1], Dawei Jiang [a,c,1], Bo Yu [b,c,d,e,1], Dalong Ni [c], Mengting Li [a,c], Yin Long [c], Paul A. Ellison [c], Cerise M. Siamof [c], Liang Cheng [f], Todd E. Barnhart [c], Hyung-Jun Im [c], Faquan Yu [e], Xiaoli Lan [a,****], Xiaohua Zhu [d,***], Qianjun He [b,**], Weibo Cai [c,g,*]

[a] Department of Nuclear Medicine, Union Hospital, Tongji Medical College, Huazhong University of Science and Technology, Wuhan, 430022, China
[b] National-Regional Key Technology Engineering Laboratory for Medical Ultrasound, Guangdong Key Laboratory for Biomedical Measurements and Ultrasound Imaging, School of Biomedical Engineering, Shenzhen University, Shenzhen, 518060, China
[c] Departments of Radiology and Medical Physics, University of Wisconsin–Madison, Madison, WI, 53705, USA
[d] Department of Nuclear Medicine, Tongji Hospital, Tongji Medical College, Huazhong University of Science and Technology, 1095 Jiefang Ave, Wuhan, 430030, China
[e] Key Laboratory for Green Chemical Process of Ministry of Education, School of Chemical Engineering and Pharmacy, Wuhan Institute of Technology, Wuhan, 430073, China
[f] Institute of Functional Nano & Soft Materials (FUNSOM), Collaborative Innovation Center of Suzhou Nano Science and Technology, Soochow University, Suzhou, 215123, China
[g] University of Wisconsin Carbone Cancer Center, University of Wisconsin–Madison, Madison, WI, 53705, USA

ARTICLE INFO

Keywords:
Nanomedicine
Acute kidney injury
Kidney targeting
Positron emission tomography (PET) imaging
Zirconium-89 (^{89}Zr)
Nuclear medicine

ABSTRACT

Acute kidney injury (AKI) leads to unacceptably high mortality due to difficulties in timely intervention and less efficient renal delivery of therapeutic drugs. Here, a series of polyvinylpyrrolidone (PVP)-curcumin nanoparticles (PCurNP) are designed to meet the renal excretion threshold (~45 kDa), presenting a controllable delivery nanosystem for kidney targeting. Renal accumulation of the relatively small nanoparticles, ^{89}Zr-PCurNP M10 with the diameter between 5 and 8 nm, is found to be 1.7 times and 1.8 times higher than the accumulation of ^{89}Zr-PCurNP M29 (20–50 nm) and M40 (20–50 nm) as revealed by PET imaging. Furthermore, serum creatinine analysis, kidney tissues histology, and tubular injury scores revealed that PCurNP M10 efficiently treated cisplatin-induced AKI. Herein, PCurNP offers a novel and simple strategy for precise PET image-guided drug delivery of renal protective materials.

1. Introduction

Kidneys perform several vital tasks including maintaining body electrolyte balance, fluid balance, and blood pressure homeostasis, primarily through the function of proximal and distal tubular segments of nephrons [1,2]. Unfortunately, according to current epidemiological evidence, the prevalence of acute and chronic renal failure is a worsening health and economic problem across the world, affecting between one and two people per thousand [3,4]. In addition, it is widely recognized that kidney injury leads to high morbidity and mortality in hospitalized patients, which was attributed to delayed diagnosis and intervention, low drug availability, treatment side effects as well as patient heterogeneity [5]. As such, new treatment regimen combining low toxicity, precise imaging, and increased therapeutic efficacy is needed to facilitate kidney disease intervention, which highlights the necessity of delivering drugs to the kidneys in a highly controllable and targeted manner.

Nanomedicine holds great promise for the targeted delivery of

Peer review under responsibility of KeAi Communications Co., Ltd.
* Corresponding authors. Departments of Radiology and Medical Physics, University of Wisconsin–Madison, Madison, WI, 53705, USA.
** Corresponding author.
*** Corresponding author.
**** Corresponding author.
E-mail addresses: xiaoli_lan@hust.edu.cn (X. Lan), evazhu@vip.sina.com (X. Zhu), nanoflower@126.com (Q. He), wcai@uwhealth.org (W. Cai).
[1] authors contributed equally.

https://doi.org/10.1016/j.bioactmat.2022.04.006
Received 22 November 2021; Received in revised form 4 April 2022; Accepted 7 April 2022

therapeutics [6]. Next to numerous reports of using nanoparticles for cancer theranostics [7], there is also clinical approval of nano-formulations for distinct diseases, including fungal infections, hepatitis, multiple sclerosis, and even end-stage renal disease [8]. However, fast liquid exchange and rapid excretion of kidneys significantly add more difficulties to targeted renal delivery [9]. For a theranostic agent to successfully localize into the kidney from the blood plasma, it must first enter the glomerulus, undergo filtration of the glomerular endothelium (with pores in the range of 80–100 nm in diameter), and pass through the glomerular basement membrane (a 300- to 350-nm-thick basal lamina), and finally go through the charged proteoglycans (an average pore size of 3 nm) [8,10]. This is a likely explanation for the fact that there are many studies reporting cancer-targeting of nanomaterials but few reporting kidney targeting. In addition, comparing with small molecule drugs, in vivo behaviours of nanoparticles involves more complex and unique physiological processes, which add more layers of complexity to renal drug delivery [11]. Excluding considerations of the shape and surface charge of theranostic agents, the molecular weight or size cut-off for glomerular filtration is thought to be 30–50 kDa or ~5 nm in diameter [12], a cut-off that obstructs the effective delivery of nanoparticles to the kidney. Therefore, despite proven successful nanoparticle delivery to cells and a few organs such as the tumours, lungs, and liver, there are few reports on efficient delivery of engineered nanoparticles to other organs, especially to the kidney [10]. Improving nanoparticle accumulation in the kidney is vital in protecting or curing renal injuries. Aside from low targeting efficiency, other limitations of nanoparticles, such as high accumulation (>30%ID/g) in the reticuloendothelial system, also lead to severe side toxicity and result in difficulties in establishing its clinical application [13]. In summary, the lack of success in translating kidney targeting nanomedicines can be attributed to the barriers of renal filtration, challenges in predicting/controlling biological profiles of nanomaterials in vivo, and drug dose management in the kidneys.

It has been well established that oxidative stress is one of the mechanisms involved in renal injury [14–17]. Thus, functional nanostructures with high biocompatibility, antioxidation, low toxicity, and specificity of targeting the kidney are of great interest in nanotechnology and medicine for potential protection or therapy on kidney injury. Numerous studies have shown that curcumin has broad biological functions, including antioxidant and anti-inflammatory properties [18,19]. For years, the information presented in research had identified curcumin as a promising renoprotective molecule [19]. The urgency to develop kidney protective strategies makes compounds like curcumin, which has been used in traditional medicine for its protective effects against renal damage, appealing.

In our previous research, both radiolabelled DNA origami nanostructures [20] and molybdenum (Mo)-based polyoxometalate clusters [21], demonstrated the possibility of antioxidative nanostructures in the prevention of AKI induced by ROS. In this work, we aimed to develop a highly selective kidney targeting nanosystem for delivering the promising renoprotective component, curcumin, to achieve the treatment of AKI. First, a series of polyvinylpyrrolidone-curcumin nanoparticles were synthesized by using polyvinylpyrrolidone (PVP) of different molecular weights (M10, M29, M40, which denote the average molecular weight of 10 kDa, 29 kDa, and 40 kDa respectively), then each was conjugated with curcumin (abbreviated as PCur M10, PCur M29, and PCur M40, respectively). The nanoparticles were formed by the hydrophobic interaction of curcumin inside the conjugates (abbreviated as PCurNP M10, PCurNP M29, and PCurNP M40, respectively) and beyond the renal excretion threshold (~45 kDa), which endowed the polyvinylpyrrolidone-curcumin conjugates biosafety nano-theranostic agents with potential applications and controllable properties for kidney targeting. The size of nanoparticles was facilely modulated by choosing PVP with different molecular weights. The nanoparticles were subsequently labeled with ^{89}Zr (abbreviated as ^{89}Zr-PCurNP M10, ^{89}Zr-PCurNP M29, and ^{89}Zr-PCurNP M40, respectively) based on the inherent oxygen donors of the polyvinylpyrrolidone-curcumin conjugates for position-emission tomography (PET) imaging. Furthermore, the as-synthesized PCurNP M10 efficiently normalized creatinine level to be 0.37 ± 0.06 mg/dL while creatinine level reached 0.87 ± 0.11 mg/dL in the cisplatin-induced AKI group. In contrast, the value of creatinine level was 0.23 ± 0.11 mg/dL in the health group. Hematoxylin and eosin (H&E) staining of the collected kidney also confirmed the successful treatment of AKI by PCurNP M10. With its attractive radiolabelling nanostructure and the simplicity of controllable kidney targeting, PCurNP offered a novel and simple strategy for precise PET image-guided drug delivery of renal protective materials-curcumin in future nanomedicine clinical studies.

2. Experimental section

2.1. Materials

Polyvinylpyrrolidone (PVP) of average molecular weight 10000, 29000 and 40000, curcumin, 4-(Dimethylamino)pyridine (DMAP), Triethylamine (TEA), Dimethyl Sulfoxide (DMSO) were purchased from Sigma-Aldrich (St. Louis, MO). 3-(4,5-Dimethylthiazol-2-yl)-2,5-diphenyltetrazolium bromide (MTT) were ordered from Thermo Fisher Scientific. Size exclusive PD-10 columns were purchased from GE Healthcare (Piscataway, NJ). Water and all buffers were of Millipore grade and pretreated with Chelex 100 resin to ensure that the aqueous solution was free of heavy metals.

2.2. Characterizations

Transmission electron microscopy (TEM) images were obtained on an FEI T12 microscope operated at an accelerating voltage of 120 kV. Standard TEM samples were prepared by dropping diluted products onto carbon-coated copper grids. Dynamic light scattering was performed on Nano-Zetasizer (Malvern Instruments Ltd.). Biodistribution studies were performed by measuring the radioactivity in the tissue in a WIZARD^2 gamma counter (Perkin-Elmer). Optical imaging was performed by using an IVIS Spectrum Preclinical in vivo imaging system (Ex = 430 nm, Em = 560 nm).

2.3. The synthesis of curcumin-polyvinyl pyrrolidone conjugates (PCur) and nanoparticles (PCurNP)

The conjugate was synthesized as reported method [22,23]. Briefly, 3 g of PVP, 1 g DMAP, 2 mL TEA, and 200 mg of curcumin were added into 100 mL of DMSO in a 250-mL flask with N_2 protection. The reaction mixture was stirred well at 45 °C for about 12 h. The resultant solution was dialyzed against DMSO for 3 days to remove unbound entities. To obtain the nanoparticles, the obtained solution dialysis against deionized water for 7 days.

2.4. Radiolabelling of PCurNPs

^{89}Zr was produced with an onsite cyclotron (GE PETrace) in the University of Wisconsin-Madison. ^{89}Zr-oxalate (150 MBq) was diluted in 300 μL of 1×10^{-3} M HEPES solution (pH ≈ 7) and mixed with 100 μL of PCurNP (M10, M29, and M40) (1 mg/mL). The reaction was conducted at 40 °C for 60 min with constant shaking. TLC determined the labeling yield at different time points. The resulting product was purified by a PD-10 column using PBS as the mobile phase.

Ga-68 (decay half-life ~ 68min) was eluted from a ^{68}Ge-^{68}Ga generator (ITG) with 0.5 N HCl (4 mL) as the mobile phase. Radiolabeling reaction starts when Ga-68, NaAc buffer (0.5 M, 300 μL, pH 6.8) and 100 μL of PCurNP (M10, M29, and M40, 1 mg/mL) were mixed together. The reaction lasts for 10–15 min with constant shaking at 37 °C and labeled nanoparticles were purified with PD-10 column (1 x PBS as the mobile phase).

2.5. In vitro serum stability study

For *in vitro* serum stability. ^{89}Zr-PCurNP M10, M29, and M40 and complete mouse serum were incubated under constant shaking at 37 °C for 24 h. Small portions of the mixture were collected at different time points and purified through 100 kDa cutoff filters. After filtering, the solutions were collected, and the radioactivity of ^{89}Zr was measured by using a gamma counter.

2.6. Animal model

All animal studies were conducted under the protocol approved by the University of Wisconsin Institutional Animal Care and Use Committee. The cisplatin-induced AKI Model model was established by intraperitoneal injections of cisplatin (15 mg/kg or 20 mg/kg) for each mouse. Then mice serum was collected to analyze creatinine levels in related groups and renal tissues were also used to assess the development of AKI and treatment of AKI by PCurNP M10. To determine the effect of PCurNP on restoring renal function, the mice were intravenously injected with PCurNP M10 (1 mg in 100 μL PBS, calculated by curcumin amount) at 2 h after intraperitoneal injections of cisplatin.

2.7. In Vivo PET imaging and biodistribution studies

The reconstruction of PET images and region-of-interest (ROI) analysis were performed similarly as described previously [24]. Briefly, for normal PET imaging, healthy BALB/c mice were each injected with 5–10 MBq of ^{89}Zr-PCurNP M10, ^{89}Zr-PCurNP M29, and ^{89}Zr-PCurNP M40, respectively via tail vein before serial PET scans. For dynamic scanning, a group of mice (n = 3) was injected with 5–10 MBq of ^{89}Zr-PCurNP. Quantitative PET data were presented as a percentage of the injected dose per gram (%ID/g). For the biodistribution study, major organs were collected and wet-weighted at 24 h postinjection. The radioactivity uptake by the tissue was measured by using a gamma counter (Perkin-Elmer) and presented as %ID/g (mean ± SD).

2.8. In vitro biocompatibility studies

The human embryonic kidney cells (HEK 293) were obtained from American Type Culture Collection (ATCC) and cultured at 37 °C under 5% CO_2. All cell culture-related reagents were purchased from Invitrogen. Cell viability was determined by measuring the ability of cells to transform MTT to a purple formazan dye. HEK 293 were incubated with PCurNP at different concentrations for 24 h then cell viability was analyzed by a microplate reader.

To measure protective effects of PCurNP, we first incubate PCurNP with HEK293 cells and challenge cells with cisplatin. MitoTrackor (ThermalFisher, USA) was used to stain mitocondria and DAPI was used to stain cell nucleus. Confocal imaging was performed on a Nikon A1R confocal microscope (Nikon Instruments, Melville, NY, USA).

2.9. In Vivo biocompatibility studies

The toxicity of nanoparticles to healthy male BALB/c mice was conducted by injecting the PCurNP M10 via the tail vein. Mice injected with only PBS were introduced as a control group (n = 3). Meanwhile, major organs from each mouse were harvested and fixed in 4% paraformaldehyde solution for 1 day. These tissues were embedded in paraffin then stained with hematoxylin and eosin (H&E) and examined using a digital microscope. Examined tissues include the heart, liver, spleen, and kidney.

2.10. Renal tissue analysis after treatment

Kidneys from each group were frozen and stored at −80 °C until experiments. Kidney homogenates were prepared according to the protocols SOD assay kits (Sigma-Aldrich, USA). For reference, SOD reference samples were used from the assay kit and a standard curve was established for our experiment.

2.11. Statistics

Quantitative data is displayed as mean ± S.D. Statistical differences were analyzed using a student's *t*-test for two groups or one-way analysis of variance (ANOVA) for three or more groups. Statistical analyses were performed using GraphPad Prism 7.

3. Results and discussion

3.1. Synthesis and ^{89}Zr-labelling of PCurNP

The synthesis of PCur was achieved by using the reported procedures [22,23]. The copolymer integration was composed of PVP and curcumin. A more detailed synthesis procedure could be found in the experimental section. The characteristics of these PCur are presented in Fig. S1, Fig. S2, Fig. S3, and Table S1. Employing the FT-IR and the UV–vis absorbance spectrometry, the curcumin composition of PCur copolymer was confirmed to be 1.23%, 1.12%, and 0.89% for PCur M10, PCur M29, and PCur M40, respectively. The nanoparticles were obtained after dialysis of reaction solution against water for one week then were purified by ultra-centrifugal filter. As-synthesized PCur nanoparticles (PCurNP) (M10, M29, and M40) showed different structures with diameters of 5–8 nm (PCurNP M10, Fig. 1A), 20-50 nm (PCurNP M29, Fig. 1B), and 20-50 nm (PCurNP M40, Fig. 1C), respectively, as observed under the transmission electron microscope (TEM) and DLS (Fig. S4).

Our previous work demonstrated that numerous deprotonated silanol groups (-O-) inside the mesochannels or on the surface of mesoporous silica nanoparticles (MSN) could function as inherent hard oxygen donors for stable radio-labeling of ^{89}Zr [24]. Based on the special structure of the synthesized PCur nanoparticles (PCurNP), we hypothesized that abundant curcumin groups might function as inherent oxygen donors for stable radiolabelling of ^{89}Zr. After mixing ^{89}Zr with the different PCurNP in HEPES buffer (0.5×10^{-3} M) at pH ≈ 7 and 45 °C for various times, the incubation solution was doted on the TLC plate for follow-up assay (Fig. S5A). It was found that the ^{89}Zr was strongly adsorbed on the nanoparticles after 5 min. And the ^{89}Zr-labelling yield of PCurNP M10, M29, and M40 reached values as high as 85.7%, 85.2%, and 85.5% respectively, after 1 h of incubation (Fig. 1D and E). Fluorescence imaging of ^{89}Zr-PCurNP (curcumin acted as the fluorescent molecule) further confirmed the nanoparticles chelated with ^{89}Zr stayed on the initial point (Fig. 1F). Furthermore, the negative control experiments with free ^{89}Zr showed a very low labeling yield, confirming the successful labeling of ^{89}Zr on the nanoparticles (Fig. S6). As shown in Fig. S7, ^{89}Zr-labeled PCurNP was stable during the co-incubation with mouse serum at 37 °C. The fractions of the obtained products were collected by purifying the mixture solutions of PCurNP and ^{89}Zr with PD-10 (Fig. S5B). A good co-localization between radioactive and fluorescence intensity of ^{89}Zr-PCurNP demonstrated the successful synthesis of ^{89}Zr- PCurNP (Fig. 1G, H, and 1I). Importantly, it was found that the PVP molecule alone could not be beneficial for labeling ^{89}Zr (Fig. 1H). Therefore, except for constructing the nanoparticles, the curcumin molecular in the polymer conjugates would also contribute to ^{89}Zr labeling.

3.2. In Vivo kidney targeting of ^{89}Zr-PCurNP

For medical applications of nanosystems, their efficacy and biosafety not only depend on the control of their distribution within the body, but also demand a clear illustration of the concentration-time profiles in organs and tissues of interest. Herein, the quantitative analysis of the dynamic PET imaging data provided more accurate biodistribution of nanoparticles in the main organs of mice. To demonstrate the kidney

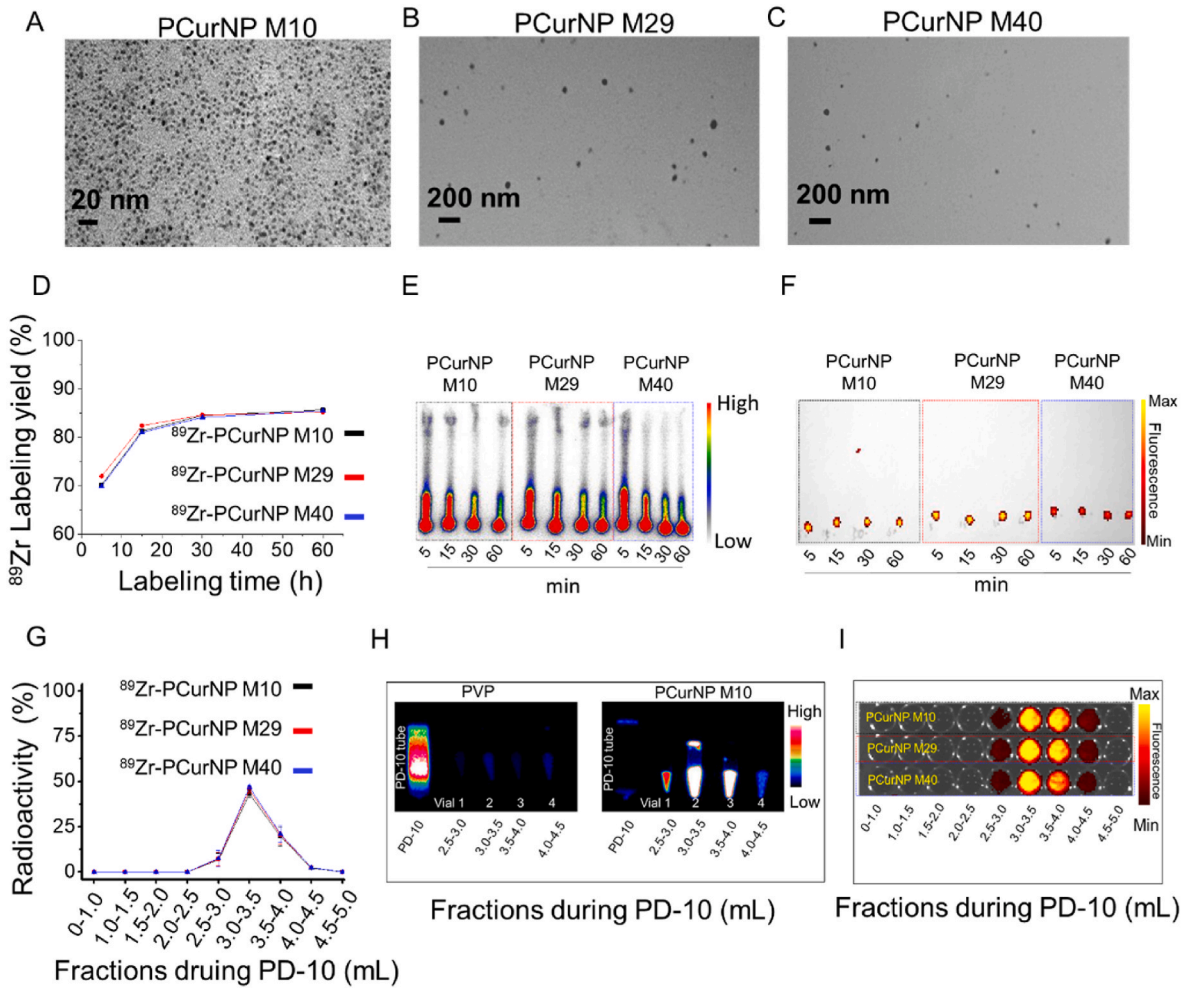

Fig. 1. Modulating the diameter and Zr-89 labeling of nanostructured polyvinylpyrrolidone-curcumin conjugates (PCur). TEM images of PCurNP M10 (**A**), M29 (**B**) and M40 (**C**). (**D**) Time-dependent ^{89}Zr-labelling yields of PCurNP (M10, M29, and M40). (**E**) Autoradiograph of TLC plates of ^{89}Zr-PCurNP. (**F**) Overlay of the bright field imaging and fluorescence of ^{89}Zr-PCurNP (Ex 430 nm, Em 530 nm). (**G**) Elution profiles based on ^{89}Zr radioactivity of ^{89}Zr-PCurNP. (**H**) PET imagines of PD-10 tubes and collected solutions from different fractions of the mixture by incubating PVP or PCurNP M10 with ^{89}Zr for 1 h. (**I**) Overlay of the bright field imaging and fluorescence of the different fractions of ^{89}Zr-PCurNP purified by PD-10.

targeting property of ^{89}Zr-PCurNP in vivo, three kinds of as-synthesized nanoparticles were intravenously injected into healthy mice and were imaged with PET at various time points post-injection. Interestingly, ^{89}Zr-PCurNP M10 with the smallest size among PCurNPs showed the most efficient kidney accumulation as compared to ^{89}Zr-PCurNP M30 and M40 (Fig. 2A, B, and C). Region-of-interest analysis of PET data and time-activity curves of the liver, blood, spleen, kidney, and muscle were shown post-injection of ^{89}Zr-PCurNP in Fig. 2D–H. Quantitative data obtained from ROI analysis of these PET images revealed that the kidney uptake of ^{89}Zr-PCurNP M10 were 15.4 ± 2.4, 15.7 ± 2.5, 15.6 ± 2.3, 14.6 ± 1.3, 11.3 ± 1.9, and 10.5 ± 1.8% ID/g at 1, 2, 3, 5, 14, and 24 h post-injection (p.i.), respectively (Fig. 2G). As demonstrated by previous research, the hydrodynamic diameter of ~5 nm or molecular weight of ~45 kDa is associated with the ability to be cleared rapidly from the body by renal filtration and urinary excretion [25]. Herein, besides the high kidney uptake, a significant signal in the bladder was attributed to the unavoidable disassembly of nanoparticles, which endowed the PCurNPs with efficient clearance ability from the body in another way. The accumulation of ^{89}Zr-PCurNP M10 in the kidney was 1.7 times and 1.8 times higher than that of ^{89}Zr-PCurNP M30 (6.3 ± 0.1% ID/g) and M40 (5.7 ± 1.2% ID/g), respectively, at 24 h time point. It was important to note that the phenomenon of radioactive signal from the kidney from three treatment groups remained unchanged in the initial 14-h post-injection: ^{89}Zr-PCurNP M10 > ^{89}Zr-PCurNP M29 > ^{89}Zr-PCurNP M40. Such an efficient selective accumulation of nanoparticles in the kidney could be due to the renal excretion threshold, ~45 kDa, which limits the uptake and retention of nanoparticles. In addition, the similar nanoparticles (PCurNP M29 and M40) got the proximate result of tissues accumulation at 24 h time point.

To estimate the uptake of nanoparticles in different organs, the mice were sacrificed with all the major organs collected, wet-weighted, and counted with a gamma counter after 24 h. Fig. 2I presented the ex vivo biodistribution of ^{89}Zr-PCurNP M10, M29, and M40 nanoparticles in mice. Numbers were given as a percentage of the injected dose (%ID/g). The dominant accumulation of nanoparticles in kidneys were found to be 15.4 ± 0.3 %ID/g (PCurNP M10), 9.2 ± 0.3 %ID/g (PCurNP M29) and 7.7 ± 1.0 %ID/g (PCurNP M40). In marked contrast, we found the three nanoparticles uptake in the liver to be 5.8 ± 0.7 %ID/g, 5.9 ± 0.5 %ID/g and 6.1 ± 0.6 %ID/g, respectively. Beside the low accumulation in the liver, the biodistribution results also showed the comparatively low value in the spleen as presented in Fig. 2I. Low signal in the liver and spleen at later time points suggested those nanoparticles can escape the uptake of mononuclear phagocytic system (MPS) cells in the reticulo-endothelial system [26]. The ability to efficiently navigate to kidneys and escape the uptake in the liver and spleen largely improved the safety and tolerability of PCurNP. In addition, the higher blood signal of PCurNP M40 signaled a longer blood circulation time than PCurNP M10. This phenomenon is likely due to the much higher molecular weight of

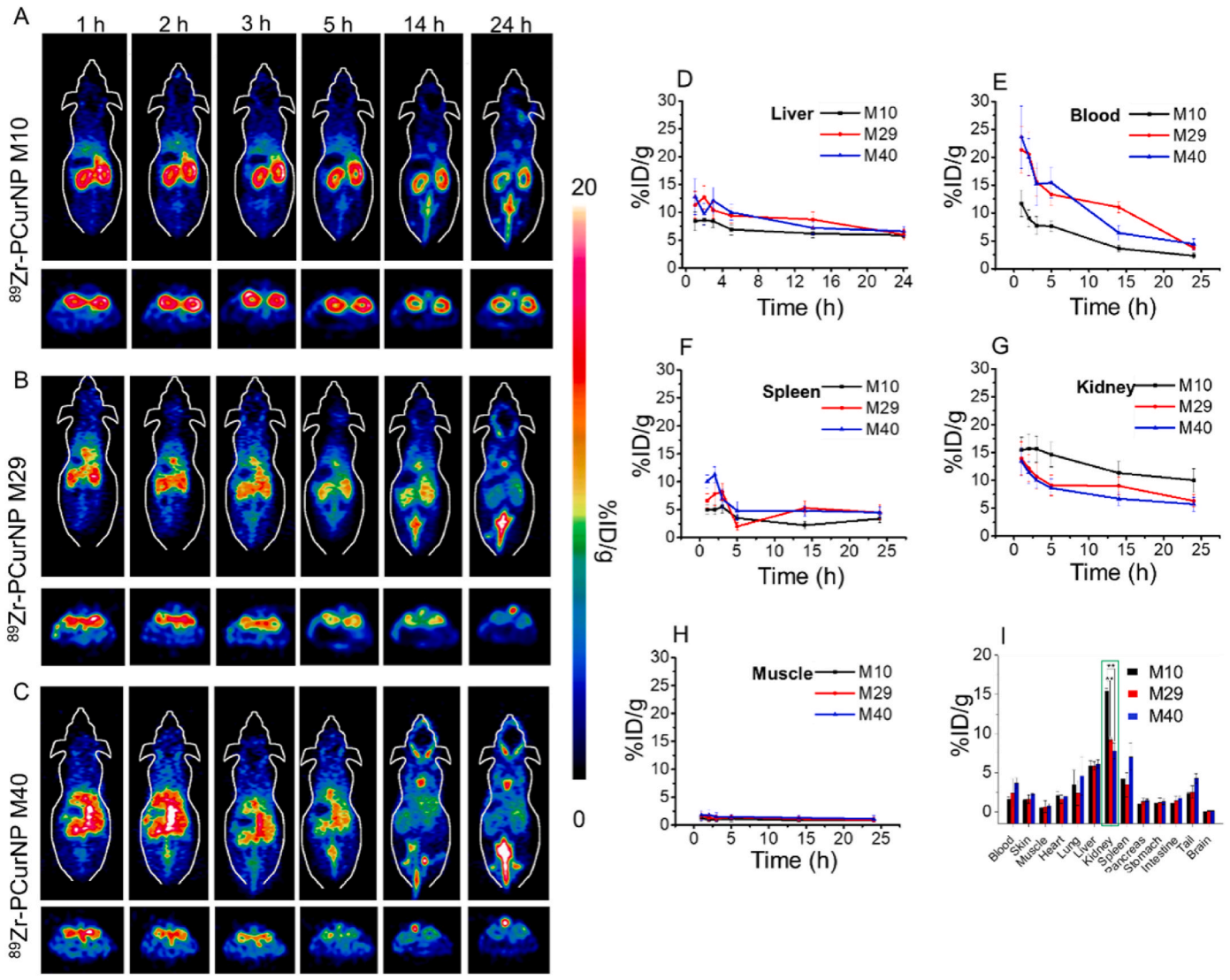

Fig. 2. *In vivo* PET images after injection of ^{89}Zr-PCurNP. *In vivo* PET images of mice taken at various time points (1, 2, 3, 5, 14, and 24 h) post intravenous injection of different ^{89}Zr-PCurNP, ^{89}Zr-PCurNP M10 (**A**), ^{89}Zr-PCurNP M29 (**B**), ^{89}Zr-PCurNP M40 (**C**). Slices that contain the kidneys are shown. Corresponding quantitative region-of-interest (ROI) analysis of ^{89}Zr-PCurNP (^{89}Zr-PCurNP M10, ^{89}Zr-PCurNP M29, ^{89}Zr-PCurNP M40) uptake in the Liver (**D**), Blood (**E**), Spleen (**F**), Kidney (**G**), and Muscle (**H**) at various time points p.i. (M10, M29, and M40 presented ^{89}Zr-PCurNP M10, ^{89}Zr-PCurNP M29, and ^{89}Zr-PCurNP M40, respectively). (**I**) Biodistribution of ^{89}Zr-PCurNP M10, M29, and M40 in the mouse at 24 h post-injection. Organ uptake was presented as %ID/g.

PVP-forming nanoparticles, which leads to a more hydrophilic layer on the surface of PCurNP M40 than for other samples. Taken together, we herein demonstrated the possibility of choosing PVP-curcumin conjugates to combine with noninvasive PET imaging for highly selective in vivo kidney mapping and targeting.

To further confirm that the size of nanoparticles would affect kidney targeting efficiency, disassembled ^{89}Zr-PCurNP M10 was obtained via incubating ^{89}Zr-PCurNP in 10% DMSO PBS solution at 37 °C for ~10 min, which was then injection into healthy mice (Fig. 3A). The structure disassembly was confirmed by the TEM imaging as shown in Fig. 3B. A significant decrease in accumulation of ^{89}Zr-PCurNP M10 was also observed in the kidney (Fig. 3C and D), in which the signal strength of radioactive signals at 24 h p.i. decreased to 6.5 ± 1.8 %ID/g (Fig. 3D). The radioactivity signal in the kidney was always weaker than the previous result (Fig. 2A) throughout the observing procedure. Another round of PET imaging was performed in mice with cisplatin-induced AKI, results showed that within 3 h after injection, PCurNP M10 nanoparticles accumulated in the kidneys with high specificity, other major organs, including the heart, liver, spleen, and lung, showed background signal (Fig. S10). These results demonstrated the potential of using ^{89}Zr-PCurNP as a PET imaging probe for in vivo kidney imaging and achieving kidney targeting by facilely choosing PVP of the proper molecular weight through systemic administration.

3.3. Dynamic PET imaging and organ kinetics of radiolabelled PCurNP

Herein, the dynamic imaging and quantitative analysis of the dynamic PET imaging data holds the potential to provide more accurate kinetics of nanoparticles in the main organs of mice without sacrificing the animals. To perform dynamic PET imaging, radiolabelled PCurNP M10 nanoparticles were injected into mice at 2–5 MBq dose and imaged in a microPET/microCT Inveon rodent model scanner. Referencing our previous work [13], a 30-min dynamic scan was performed and fitted into several frames. Fig. 4A showed the selected frames of maximum intensity projection (MIP) images from the dynamic PET imaging, which showed the rapid decrease of ^{89}Zr-PCurNP M10 in the blood during the first 30 min after injecting into healthy mice. The results showed an instant uptake (36.4 ± 13.9 %ID/g) of ^{89}Zr-PCurNP M10 in the kidney at 2.25 min post-injection and then decreased to 16.7 ± 4.6 %ID/g at the 30-min time point. By comparing the kidney time-activity curves of

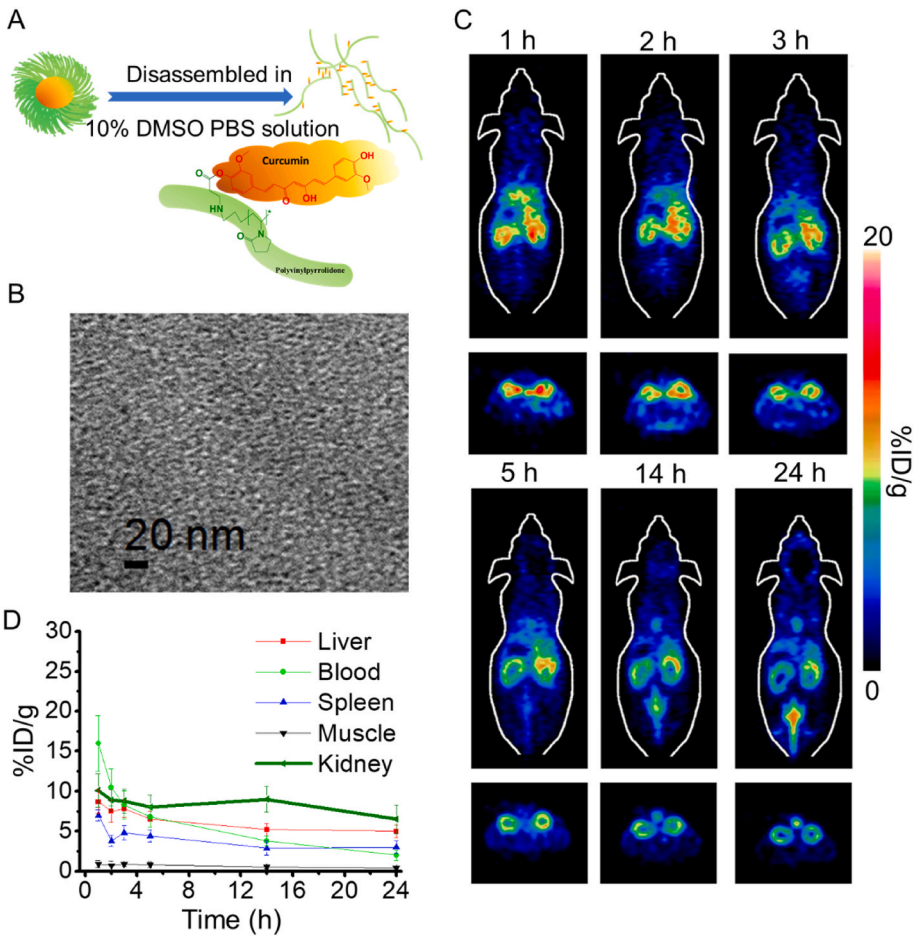

Fig. 3. (**A**) A schematic illustration showed the disassembly of ^{89}Zr-PCurNP M10 via incubating the obtained ^{89}Zr-PCurNP in 10% DMSO PBS solution at 37 °C for ~10 min. (**B**) TEM imaging of the disassembled ^{89}Zr-PCurNP M10. (**C**) Quantification of the disassembled ^{89}Zr-PCurNP M10 uptake in the Liver, Spleen, Muscle, and Kidney at various time points p.i. The unit is the percentage of injected dose per gram of tissue (% ID/g). (**D**) *In Vivo* PET imaging after injection of the disassembled ^{89}Zr-PCurNP M10, where the slices that contain the kidneys are shown.

^{89}Zr-PCurNP M10 and ^{89}Zr-PCurNP M40 (Figs. S8 and S9), dynamic PET results showed the blood circulation of ^{89}Zr-PCurNP M40 was longer than that of ^{89}Zr-PCurNP M10, while the opposite result was found in the kidney uptake of two nanoparticles. The spleen and liver uptake of the two nanoparticles showed similar results. These data matched quite well with the obtained trend from our ex vivo biodistribution study. Uptake of ^{89}Zr-PCurNP M10 in the liver was measured to be at a maximum value of 22.2 ± 9.1 %ID/g and kept in the low value throughout the scanning procedure. The signal in the spleen increased to 14.4 ± 2.2 %ID/g at 13 min time point before it started to decrease over time. As was previously reported [27], radioactivity signal in the bladder could likely be partly due to the small amount of free ^{89}Zr that was not completely removed before injection, allowing it to become concentrated in the bladder after intravenous injection. Fig. 4B–E shows the detailed time-activity curves of ^{89}Zr-PCurNP M10 in the heart, kidneys, liver, and spleen. The distribution rate of ^{89}Zr-PCurNP M10 from the blood compartment was later determined by fitting the dynamic time-activity curves of the heart to a two-phase exponential decay (showed Fig. 4F). The initial distribution half-life ($t_{1/2\alpha}$) of the ^{89}Zr-PCurNP M10 was found to be 0.16 ± 0.16 min and was confirmed with the rapid distribution of nanoparticles as showed in Fig. 4A. In addition, the elimination half-life ($t_{1/2\beta}$), obtained by fitting the time-activity curve, was 6.64 ± 0.42 min. The initial distribution and elimination half-life of ^{89}Zr-PCurNP M10 in the liver was estimated to be similar to the heart, suggests that ^{89}Zr-PCurNP M10 can rapidly accumulate in the kidney and can also be rapidly cleared by the mice.

3.4. Biocompatibility evaluations of PCurNP

According to the above results, synthesized nanoparticles mainly accumulated in the kidney. Herein, human embryonic kidney cells 293 (HEK-293) were chosen as model cells to evaluate the biocompatibility of PCurNP. No apparent cytotoxicity of PCurNP M10, M29, and M40 to HEK-293 was observed at a studied concentration (from 62.5 to 1000 μg/mL) up to 24 h (Fig. 5A). To further confirm its biosafety, PCurNP M10 was injected into the healthy Balb/c mice at the dose of 15 mg/kg. No noticeable signs of toxicity or side effects were found in the Balb/c mice based on the bodyweight measurement (Fig. 5B). On Day 30, major organs (i.e., heart, liver, spleen, kidneys) were sliced and stained with H&E for histology analysis. The results in Fig. 5C further revealed that there was no noticeable tissue damage in any of the main organs of the healthy mice. Combined with retention information acquired from PET imaging, it is reasonable to conclude that this nanosized conjugates would not cause significant toxicity to the test subjects.

3.5. Treatment of cisplatin-induced AKI with PCurNP

Among the chemotherapeutic agents, cisplatin is a widely used anticancer drug. However, one of the main concerns of cisplatin administration is acute kidney injury (AKI) [28]. Effective management of cisplatin-induced AKI would be promising to move the cisplatin-based anticancer strategy forward. Herein, being inspired by the kidney targeting property of PCurNP, we sought to determine if kidney targeted delivery of curcumin contained nanoconjugates could restore the renal function in cisplatin-induced AKI. As shown in Fig. 6A, AKI treatment using PCurNP M10 efficiently normalized serum creatinine level to be 0.37 ± 0.06 mg/dL (0.23 ± 0.11 mg/dL in health mice), while the value reached 0.87 ± 0.11 mg/dL in the group of cisplatin (15 mg/kg) induced AKI. Blood urine nitrogen (BUN) test also confirmed the alleviated kidney damage (Fig. 6B). When increasing the cisplatin concentration

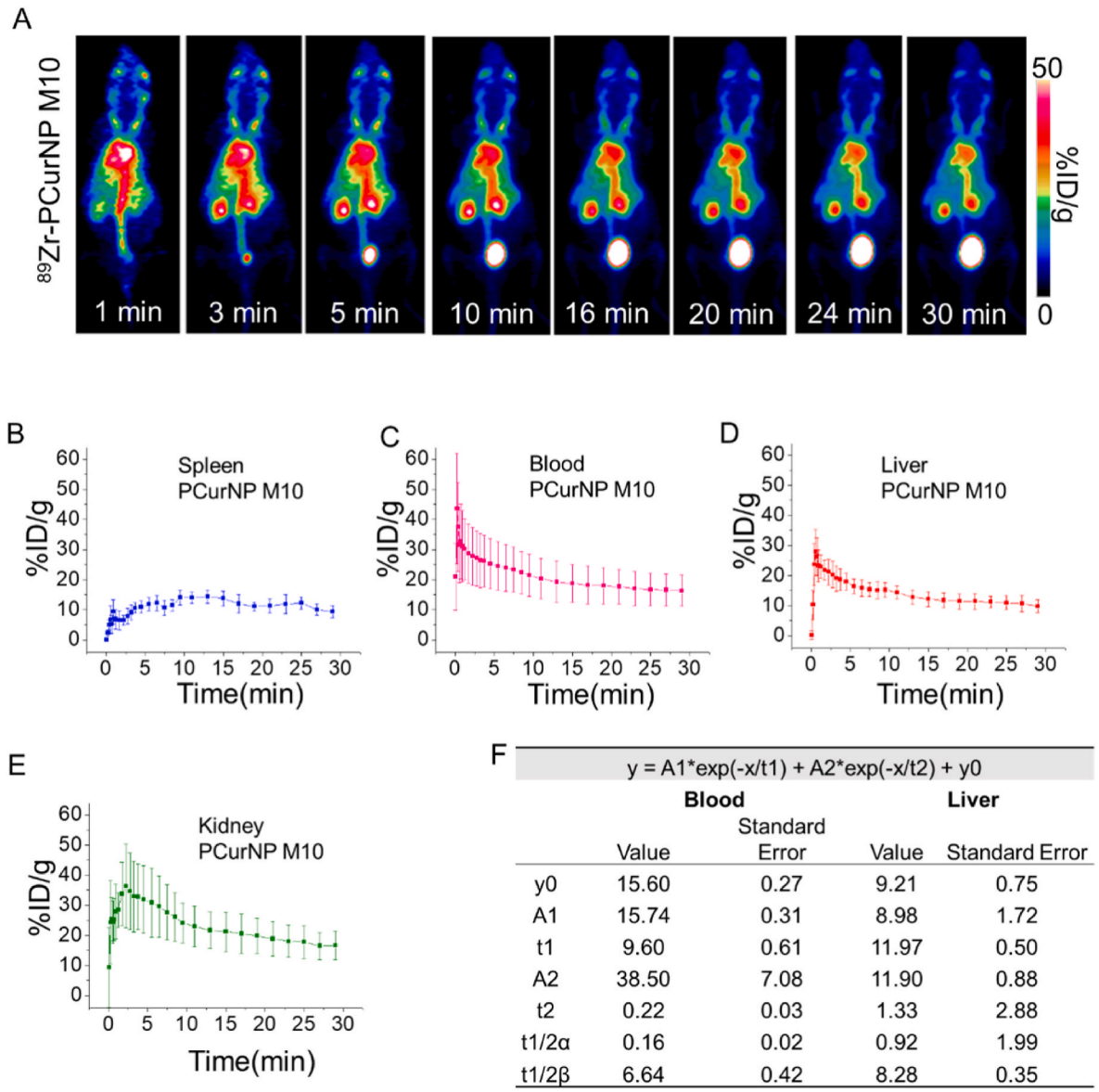

F

$y = A1*\exp(-x/t1) + A2*\exp(-x/t2) + y0$

	Blood		Liver	
	Value	Standard Error	Value	Standard Error
y0	15.60	0.27	9.21	0.75
A1	15.74	0.31	8.98	1.72
t1	9.60	0.61	11.97	0.50
A2	38.50	7.08	11.90	0.88
t2	0.22	0.03	1.33	2.88
t1/2α	0.16	0.02	0.92	1.99
t1/2β	6.64	0.42	8.28	0.35

Fig. 4. (**A**) Dynamic PET imaging. Selected frames showing the maximum intensity projection (MIP) images from dynamic PET imaging of mice injected with ^{89}Zr-PCurNP M10. Time-activity curves of ^{89}Zr-PCurNP M10 in different major organs of Spleen (**B**), Blood (**C**), Liver (**D**), and Kidney (**E**). (**F**) A table summarized the two-compartment model fitting result of ^{89}Zr-PCurNP M10 in heart and liver.

(20 mg/kg), the creatinine level of tested animals was higher than 1 mg/dL. In this case, PCurNP did not show the ability to reduce creatinine levels (creatinine value was > 1 mg/dL). According to the histology results (Fig. 6C, **D** and Fig. S11), the renal tubular cells indicated necrosis (blue arrows 1) and shed into the lumen (red arrows 2), exposing the tubular basement membrane (green arrows 3). Also, large amounts of colloidal protein tubules in renal tubules were confirmed and the tubular revealed dilatation and protein casts (asterisk). The tubular injury score also confirmed the successfully restored renal function by using PCurNP M10 to treat cisplatin-induced AKI (Fig. 6E). To further evaluate the role of PCurNP-delivered curcumin for AKI alleviation, we tested superoxide dismutase (SOD) levels in the kidneys. Results showed that AKI animals without treatment displayed severely decreased levels of SOD, suggesting deteriorating kidney function and loss of oxidative hemostasis as a result of cisplatin. After treatment with PcurNP M10, renal SOD levels increased significantly, reaching levels similar to healthy mice (Fig. S12). Cellular studies verified our in vivo observation, when challenged with cisplatin, HEK293 cells showed severely damaged mitocondria, which were mostly intact when protected with PCurNPs (Fig. S13). Thus, our result indicated the potential of PCurNP M10 to restore renal function in AKI mice induced by low concentration cisplatin.

Recently, there are reports indicating that macrophage-myofibroblast transition is involved in the progression of chronic kidney [29,30], and lung [31] diseases. In our current study, we did not observe any involvement of renal fibrosis due to the acuteness of kidney injury and the short time window of treatment. In the future, the investigation of macrophage-myofibroblast transition in an extended period of renal injury models would strengthen our knowledge in kidney-disease treatment with PCurNPs.

4. Conclusions

Herein, we report the successful synthesis of radiolabelled PCurNPs with controllable kidney-targeting properties as revealed by dynamic PET imaging. In murine models of cisplatin-induced AKI, the size-dependent kidney accumulation of PCurNPs efficiently delivered curcumin to alleviate renal damage and restore kidney function after

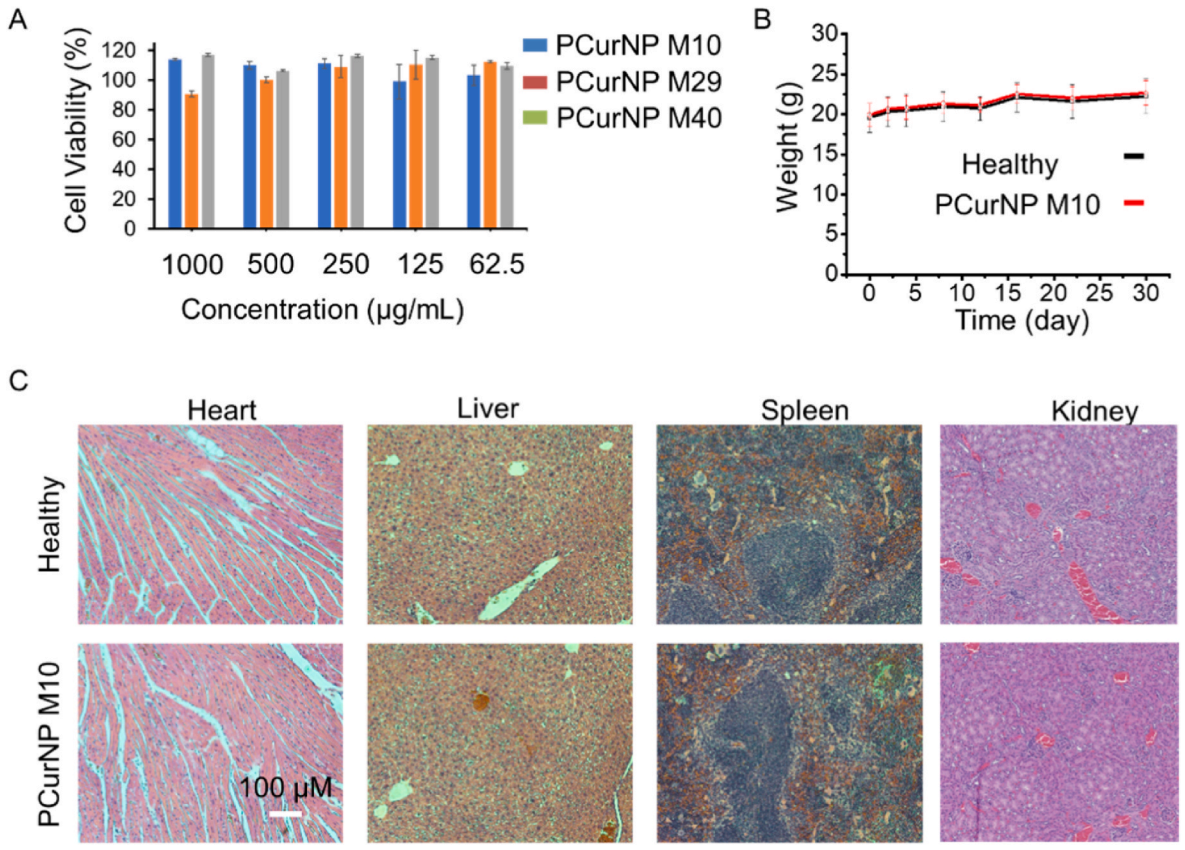

Fig. 5. Biocompatibility study. (**A**) Toxicity of PCurNP toward HEK293 cells (24 h). (**B**) Growth chart of mice post-treatment of PCurNP M10. (**C**) H&E stained major organ slides collected from healthy Balb/c mice and PCurNP M10-injected mice (dose: 15 mg/kg) on day 30 post-injection. Scale bar: 100 μm.

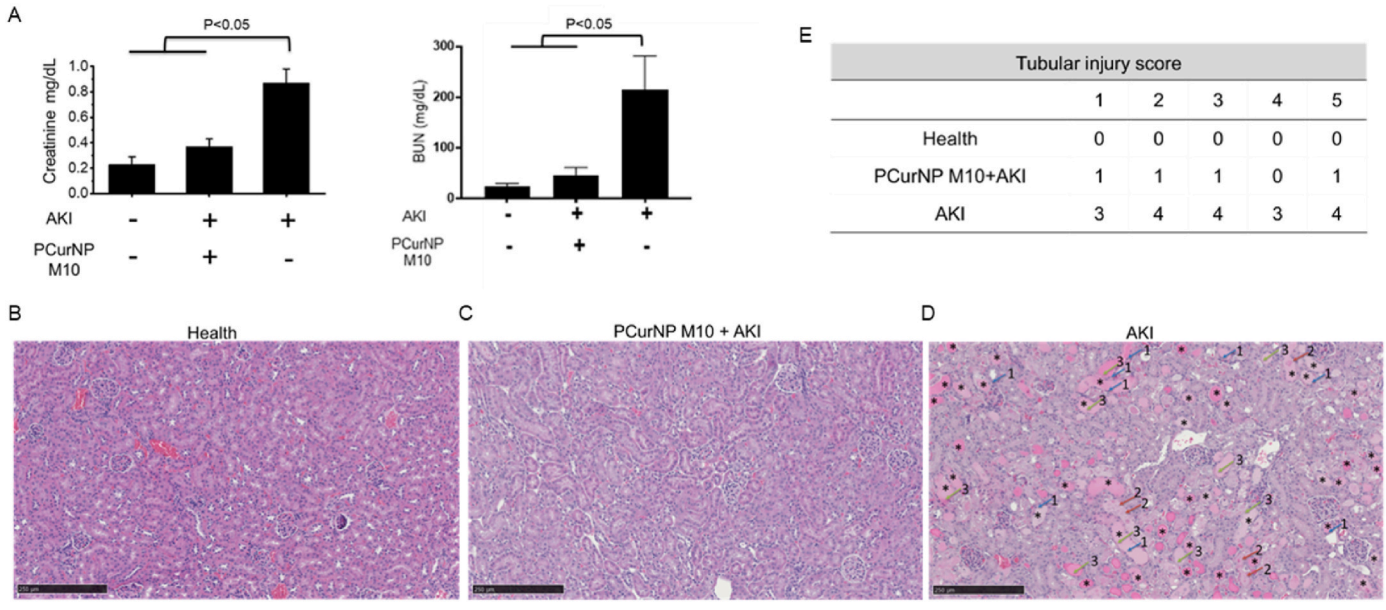

Fig. 6. (A) Creatinine and blood urine nitrogen (BUN) levels of tested animals in the groups of control, cisplatin-induced AKI, PCurNP M10 treatment of cisplatin-induced AKI. (B, C, D) Histology analysis of collected renal tissues in each group. Cisplatin induced AKI denoted as AKI. (E) Scoring of tubular injury (n = 3–4). The injuries of tubules were graded from 0 to 4 as follows: 0 represents no lesion, 1 represents areas of tubular epithelial cells (TECs) swelling, vacuolar degeneration, necrosis and the loss of brush border involving <25% of cortical tubules; and 2, 3, and 4 indicating the percentage of tubular damage is 25%–50%, 50%–75%, and more than 75% of the cortical tubules, respectively.

cisplatin insult. We believe PCurNP offers a novel and simple strategy for PET image-guided renal delivery of anti-inflammatory and anti-oxidant drugs (such as curcumin in this study) and may find broader use in preclinical nanomedicine and clinical translation.

CRediT authorship contribution statement

Hao Wei: Conceptualization, Investigation, Methodology, Validation, Writing – original draft. **Dawei Jiang:** Conceptualization, Investigation, Methodology, Validation, Writing – original draft. **Bo Yu:** Conceptualization, Investigation, Methodology, Validation, Funding acquisition, Writing – original draft. **Dalong Ni:** Investigation, Methodology, Validation. **Mengting Li:** Investigation, Methodology, Validation. **Yin Long:** Investigation, Methodology, Validation. **Paul A. Ellison:** Investigation, Methodology, Validation. **Cerise M. Siamof:** Methodology, Validation. **Liang Cheng:** Investigation, Methodology, Validation. **Todd E. Barnhart:** Investigation, Methodology, Validation. **Hyung-Jun Im:** Investigation, Methodology, Validation. **Faquan Yu:** Investigation, Methodology, Validation. **Xiaoli Lan:** Validation, Conceptualization, Supervision, Writing – review & editing. **Xiaohua Zhu:** Validation, Conceptualization, Supervision, Writing – review & editing. **Qianjun He:** Validation, Conceptualization, Funding acquisition, Supervision, Writing – review & editing. **Weibo Cai:** Validation, Conceptualization, Funding acquisition, Supervision, Writing – review & editing.

Declaration of competing interest

The authors declare no known competing financial interests or personal relationships that could have appeared to influence the work reported in this paper.

Acknowledgments

This work was supported by the National Natural Science Foundation of China (81601605, 21571147, 82102121) and the Postdoctoral Science Foundation of China (2016M600670). This work was also supported by the University of Wisconsin–Madison, the National Institutes of Health (NIBIB/NCI P30CA014520), the Natural Science Foundation of SZU (Grant No. 827-000143), and the Shenzhen Peacock Plan (KQTD20160531122051497).

Appendix A. Supplementary data

Supplementary data to this article can be found online at https://doi.org/10.1016/j.bioactmat.2022.04.006.

References

[1] A.S. Go, G.M. Chertow, D. Fan, C.E. McCulloch, C.-y. Hsu, Chronic kidney disease and the risks of death, cardiovascular events, and hospitalization, N. Engl. J. Med. 351 (13) (2004) 1296–1305, https://doi.org/10.1056/NEJMoa041031.

[2] H. Huang, R. Hernandez, J. Geng, H. Sun, W. Song, F. Chen, S.A. Graves, R. J. Nickles, C. Cheng, W. Cai, A porphyrin-PEG polymer with rapid renal clearance, Biomaterials 76 (2016) 25–32, https://doi.org/10.1016/j.biomaterials.2015.10.049.

[3] A.M. El Nahas, A.K. Bello, Chronic kidney disease: the global challenge, Lancet 365 (9456) (2005) 331–340, https://doi.org/10.1016/S0140-6736(05)17789-7.

[4] A.S. Levey, J. Coresh, Chronic kidney disease, Lancet 379 (9811) (2012) 165–180, https://doi.org/10.1016/S0140-6736(11)60178-5. Epub 2011 Aug 15.

[5] S.K. Jo, M.H. Rosner, M.D. Okusa, Pharmacologic treatment of acute kidney injury: why drugs haven't worked and what is on the horizon, Clin. J. Am. Soc. Nephrol. 2 (2) (2007) 356–365, https://doi.org/10.2215/CJN.03280906.

[6] T.C. Johnstone, K. Suntharalingam, S.J. Lippard, The next generation of platinum drugs: targeted Pt (II) agents, nanoparticle delivery, and Pt (IV) prodrugs, Chem. Rev. 116 (5) (2016) 3436–3486, https://doi.org/10.1021/acs.chemrev.5b00597.

[7] K. Cho, X. Wang, S. Nie, D.M. Shin, Therapeutic nanoparticles for drug delivery in cancer, Clin. Cancer Res. 14 (5) (2008) 1310–1316, https://doi.org/10.1158/1078-0432.CCR-07-1441.

[8] E. Blanco, H. Shen, M. Ferrari, Principles of nanoparticle design for overcoming biological barriers to drug delivery, Nat. Biotechnol. 33 (9) (2015) 941–951, https://doi.org/10.1038/nbt.3330.

[9] R. Mout, D.F. Moyano, S. Rana, V.M. Rotello, Surface functionalization of nanoparticles for nanomedicine, Chem. Soc. Rev. 41 (7) (2012) 2539–2544, https://doi.org/10.1039/c2cs15294k.

[10] C.H.J. Choi, J.E. Zuckerman, P. Webster, M.E. Davis, Targeting kidney mesangium by nanoparticles of defined size, Proc. Natl. Acad. Sci. U.S.A. 108 (16) (2011) 6656–6661, https://doi.org/10.1073/pnas.1103573108. Epub 2011 Apr 4.

[11] X. Liang, H. Wang, J.E. Grice, L. Li, X. Liu, Z.P. Xu, M.S. Roberts, Physiologically based pharmacokinetic model for long-circulating inorganic nanoparticles, Nano Lett. 16 (2) (2016) 939–945, https://doi.org/10.1021/acs.nanolett.5b03854.

[12] A. Ruggiero, C.H. Villa, E. Bander, D.A. Rey, M. Bergkvist, C.A. Batt, K. Manova-Todorova, W.M. Deen, D.A. Scheinberg, M.R. McDevitt, Paradoxical glomerular filtration of carbon nanotubes, Proc. Natl. Acad. Sci. U.S.A. 107 (27) (2010) 12369–12374, https://doi.org/10.1073/pnas.0913667107. Epub 2010 Jun 21.

[13] F. Chen, S. Goel, R. Hernandez, S.A. Graves, S. Shi, R.J. Nickles, W. Cai, Dynamic positron emission tomography imaging of renal clearable gold nanoparticles, Small 12 (20) (2016) 2775–2782, https://doi.org/10.1002/smll.201600194. Epub 2016 Apr 9.

[14] J. Kim, Y.M. Seok, K.-J. Jung, K.M. Park, Reactive oxygen species/oxidative stress contributes to progression of kidney fibrosis following transient ischemic injury in mice, Am. J. Physiol. Ren. Physiol. 297 (2) (2009) F461–F470, https://doi.org/10.1152/ajprenal.90735.2008. Epub 2009 May 20.

[15] G.-S. Oh, H.-J. Kim, J.-H. Choi, A. Shen, S.-K. Choe, A. Karna, S.H. Lee, H.-J. Jo, S.-H. Yang, T.H. Kwak, Pharmacological activation of NQO1 increases NAD+ levels and attenuates cisplatin-mediated acute kidney injury in mice, Kidney Int. 85 (3) (2014) 547–560, https://doi.org/10.1038/ki.2013.330. Epub 2013 Sep. 11.

[16] D. Xu, M. Chen, X. Ren, X. Ren, Y. Wu, Leonurine ameliorates LPS-induced acute kidney injury via suppressing ROS-mediated NF-κB signaling pathway, Fitoterapia 97 (2014) 148–155, https://doi.org/10.1016/j.fitote.2014.06.005. Epub 2014 Jun 9.

[17] H. Yu, T. Lin, W. Chen, W. Cao, C. Zhang, T. Wang, M. Ding, S. Zhao, H. Wei, H. Guo, X. Zhao, Size and temporal-dependent efficacy of oltipraz-loaded PLGA nanoparticles for treatment of acute kidney injury and fibrosis, Biomaterials 219 (2019) 119368, https://doi.org/10.1016/j.biomaterials.2019.119368.

[18] J. Barry, M. Fritz, J.R. Brender, P.E. Smith, D.-K. Lee, A. Ramamoorthy, Determining the effects of lipophilic drugs on membrane structure by solid-state NMR spectroscopy: the case of the antioxidant curcumin, J. Am. Chem. Soc. 131 (12) (2009) 4490–4498, https://doi.org/10.1021/ja809217u.

[19] J. Trujillo, Y.I. Chirino, E. Molina-Jijón, A.C. Andérica-Romero, E. Tapia, J. Pedraza-Chaverrí, Renoprotective effect of the antioxidant curcumin: recent findings, Redox Biol. 1 (1) (2013) 448–456, https://doi.org/10.1016/j.redox.2013.09.003.

[20] D. Jiang, Z. Ge, H.J. Im, C.G. England, D. Ni, J. Hou, L. Zhang, C.J. Kutyreff, Y. Yan, Y. Liu, S.Y. Cho, J.W. Engle, J. Shi, P. Huang, C. Fan, H. Yan, W. Cai, DNA origami nanostructures can exhibit preferential renal uptake and alleviate acute kidney injury, Nat. Biomed. Eng. 2 (11) (2018) 865–877, https://doi.org/10.1038/s41551-018-0317-8.

[21] D. Ni, D. Jiang, C.J. Kutyreff, J. Lai, Y. Yan, T.E. Barnhart, B. Yu, H.J. Im, L. Kang, S.Y. Cho, Z. Liu, P. Huang, J.W. Engle, W. Cai, Molybdenum-based nanoclusters act as antioxidants and ameliorate acute kidney injury in mice, Nat. Commun. 9 (1) (2018) 5421, https://doi.org/10.1038/s41467-018-07890-8.

[22] S. Manju, K. Sreenivasan, Enhanced drug loading on magnetic nanoparticles by layer-by-layer assembly using drug conjugates: blood compatibility evaluation and targeted drug delivery in cancer cells, Langmuir 27 (23) (2011) 14489–14496, https://doi.org/10.1021/la202470k. Epub 2011 Oct 27.

[23] B. Yu, X. Li, W. Zheng, Y. Feng, Y.-S. Wong, T. Chen, pH-responsive cancer-targeted selenium nanoparticles: a transformable drug carrier with enhanced theranostic effects, J. Mater. Chem. B 2 (33) (2014) 5409–5418, https://doi.org/10.1039/c4tb00399c.

[24] F. Chen, S. Goel, H.F. Valdovinos, H. Luo, R. Hernandez, T.E. Barnhart, W. Cai, In vivo integrity and biological fate of chelator-free zirconium-89-labeled mesoporous silica nanoparticles, ACS Nano 9 (8) (2015) 7950–7959, https://doi.org/10.1021/acsnano.5b00526.

[25] H.S. Choi, W. Liu, P. Misra, E. Tanaka, J.P. Zimmer, B.I. Ipe, M.G. Bawendi, J. V. Frangioni, Renal clearance of quantum dots, Nat. Biotechnol. 25 (10) (2007) 1165–1170, https://doi.org/10.1038/nbt1340. Epub 2007 Sep. 23.

[26] X. Xu, W. Ho, X. Zhang, N. Bertrand, O. Farokhzad, Cancer nanomedicine: from targeted delivery to combination therapy, Trends Mol. Med. 21 (4) (2015) 223–232, https://doi.org/10.1016/j.molmed.2015.01.001. Epub 2015 Feb 2.

[27] L. Cheng, A. Kamkaew, S. Shen, H.F. Valdovinos, H. Sun, R. Hernandez, S. Goel, T. Liu, C.R. Thompson, T.E. Barnhart, Facile preparation of multifunctional WS2/WOx nanodots for chelator-free 89Zr-labeling and in vivo PET imaging, Small 12 (41) (2016) 5750–5758, https://doi.org/10.1002/smll.201601696. Epub 2016 Sep. 4.

[28] S.J. Holditch, C.N. Brown, A.M. Lombardi, K.N. Nguyen, C.L. Edelstein, Recent advances in models, mechanisms, biomarkers, and interventions in cisplatin-induced acute kidney injury, Int. J. Mol. Sci. 20 (12) (2019), https://doi.org/10.3390/ijms20123011.

[29] P.M. Tang, Y.Y. Zhang, J. Xiao, P.C. Tang, J.Y. Chung, J. Li, V.W. Xue, X.R. Huang, C.C. Chong, C.F. Ng, T.L. Lee, K.F. To, D.J. Nikolic-Paterson, H.Y. Lan, Neural transcription factor Pou4f1 promotes renal fibrosis via macrophage-myofibroblast transition, Proc. Natl. Acad. Sci. U.S.A. 117 (34) (2020) 20741–20752, https://doi.org/10.1073/pnas.1917663117.

[30] Á. Torres, K. Muñoz, Y. Nahuelpán, R.S. Ap, P. Mendoza, C. Jara, C. Cappelli, R. Suarez, C. Oyarzún, C. Quezada, R. San Martín, Intraglomerular monocyte/macrophage infiltration and macrophage-myofibroblast transition during diabetic nephropathy is regulated by the A(2B) adenosine receptor, Cells 9 (4) (2020), https://doi.org/10.3390/cells9041051.

[31] F. Yang, Y. Chang, C. Zhang, Y. Xiong, X. Wang, X. Ma, Z. Wang, H. Li, T. Shimosawa, L. Pei, Q. Xu, UUO induces lung fibrosis with macrophage-

myofibroblast transition in rats, Int. Immunopharm. 93 (2021), 107396, https://doi.org/10.1016/j.intimp.2021.107396.